Cell Reports
Physical Science

CellPress
OPEN ACCESS

Article

Enhancing the electrochemical reduction of carbon dioxide to multi-carbon products on copper nanosheet arrays via cation-catalyst interaction

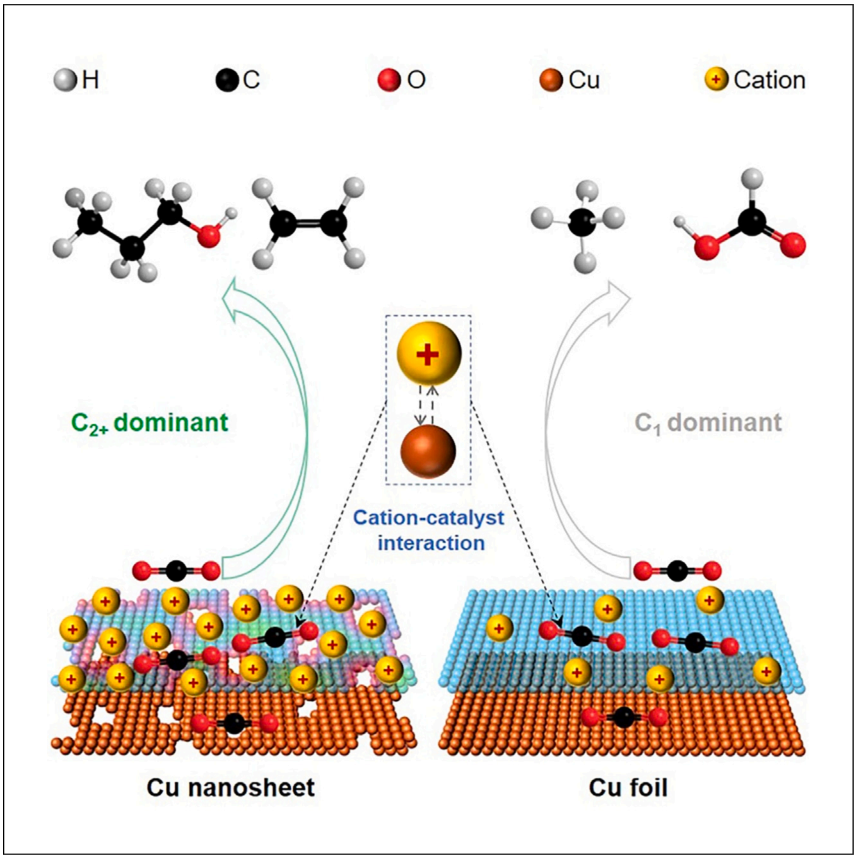

Here, Yu et al. prepare copper nanosheet arrays with unconventional orientation via an *in situ* electrochemical method. Using optimized cation-catalyst interactions, the copper nanosheets exhibit a Faradaic efficiency of 53.6% toward ethylene and a high multi-carbon to single-carbon ratio in electrochemical carbon dioxide reduction, which are better than the performance of bare copper foil.

Jinli Yu, Mingzi Sun, Juan Wang, ..., Chun-Sing Lee, Bolong Huang, Zhanxi Fan

bhuang@polyu.edu.hk (B.H.)
zhanxi.fan@cityu.edu.hk (Z.F.)

Highlights

Copper nanosheet arrays mainly enclosed by {100} facets are prepared

The multi-carbon to single-carbon ratio is higher on nanosheets than on bare foils

The density of adsorbed potassium ions is enhanced on the copper nanosheets

Adsorbed potassium ions lower the energy barrier for converting CO_2 to C_{2+} products

Yu et al., Cell Reports Physical Science 4, 101366
April 19, 2023 © 2023 The Author(s).
https://doi.org/10.1016/j.xcrp.2023.101366

Cell Reports
Physical Science

CellPress
OPEN ACCESS

Article

Enhancing the electrochemical reduction of carbon dioxide to multi-carbon products on copper nanosheet arrays via cation-catalyst interaction

Jinli Yu,[1,6] Mingzi Sun,[3,6] Juan Wang,[1,6] Yunhao Wang,[1,6] Yang Li,[1,6] Pengyi Lu,[1,2] Yangbo Ma,[1] Jingwen Zhou,[1,2] Wenze Chen,[1] Xichen Zhou,[1] Chun-Sing Lee,[1] Bolong Huang,[3,5,*] and Zhanxi Fan[1,2,4,7,*]

SUMMARY

Electrochemical carbon dioxide reduction offers an efficient way to curtail carbon emissions and generate value-added chemicals and fuels. However, this reaction still suffers from sluggish kinetics and poor selectivity, especially for the formation of multi-carbon products. Here, we report the preparation of copper nanosheet arrays mainly enclosed by {100} facets on copper foils. The copper nanosheets promote the formation of multi-carbon products with a multi-carbon to single-carbon ratio of 7.2, which is almost 18 times that of bare copper foils. Electrochemical investigations reveal that the density of adsorbed potassium ions on copper nanosheet surfaces is approximately five times that on pristine copper foils. Theoretical calculations indicate that the adsorbed potassium ions can effectively modulate the electronic structures of copper nanosheets and thus lower the energy barriers for highly selective generation of multi-carbon products. This work highlights the substantial implications of cation-catalyst interactions for multi-carbon production in electrochemical carbon dioxide reduction reaction.

INTRODUCTION

The fast-growing amount of CO_2 in the global atmosphere poses a huge threat to the living environment of humans,[1] which has motivated researchers in different fields to develop effective technologies to tackle CO_2 emission problems.[2–8] In this regard, the electrochemical CO_2 reduction reaction (CO_2RR) is considered one of the most promising techniques, as it can upgrade CO_2 to value-added fuels and chemical feedstocks by utilizing renewable electricity.[9–12] Currently, Cu-based catalysts show very unique selectivity in the electrochemical CO_2RR because they can facilitate the generation of multi-carbon (C_{2+}) products (e.g., ethylene [C_2H_4], ethanol [C_2H_5OH], and n-propanol [n-C_3H_7OH]) with considerable Faradaic efficiency (FE), which are much more valuable than the single-carbon (C_1) products (e.g., formic acid [HCOOH] and carbon monoxide [CO]).[13–17] To enhance the CO_2RR performance, great research efforts have been devoted to developing novel Cu-based catalysts with different strategies, including the control of morphology, composition, size, facet, crystal phase, oxidation state, and defect, as well as the surface functionalization.[18–26] Besides, reaction environment modulation (e.g., electrolytes, local pH, and mass transfer) and cell design (e.g., H-type cell, gaseous cell, and flow cell) were also extensively explored to improve the overall CO_2-reduction performance.[27–31] However, although significant progress have been achieved,

---

[1] Department of Chemistry, City University of Hong Kong, Hong Kong, SAR 999077, China

[2] Hong Kong Branch of National Precious Metals Material Engineering Research Center (NPMM), City University of Hong Kong, Hong Kong, SAR 999077, China

[3] Department of Applied Biology and Chemical Technology, The Hong Kong Polytechnic University, Hung Hom, Kowloon, Hong Kong, SAR 999077, China

[4] Shenzhen Research Institute, City University of Hong Kong, Shenzhen 518057, China

[5] Research Centre for Carbon-Strategic Catalysis, The Hong Kong Polytechnic University, Hung Hom, Kowloon, Hong Kong, SAR 999077, China

[6] These authors contributed equally

[7] Lead contact

*Correspondence: bhuang@polyu.edu.hk (B.H.), zhanxi.fan@cityu.edu.hk (Z.F.)

https://doi.org/10.1016/j.xcrp.2023.101366

Cu-based catalysts still suffer severely from their insufficient activity and limited selectivity toward the electrochemical CO_2RR, especially for the formation of high-value C_{2+} products.

Recently, cation engineering has emerged as an efficient approach to boost the performance of the electrochemical CO_2RR. In general, cations can suppress the competitive hydrogen evolution reaction (HER), tune the selectivity, and adjust the reaction rate of the CO_2RR.[32–35] To date, several mechanisms have been proposed to rationalize the aforementioned cation effects, including tuning the structure of the electrochemical double layer (EDL), buffering the local pH, modulating the interfacial electric field, and interacting with the reaction intermediates.[36–40] Since the cations can interact with the intermediates and affect their electronic structures, it is deduced that the cations could also interact with the surface atoms of catalysts under negative bias and change their electronic structures if the cations are attracted close enough to the surface of the electrode. In particular, previous studies have revealed that specifically adsorbed cations on the catalysts can affect the electronic structure of their surface atoms, thereby modulating the catalytic property.[41–45] Significantly, Waegele et al. recently observed that the coverage of specifically adsorbed alkali metal cations on an Au electrode during CO_2-to-CO reduction follows the order of $Li^+ < Na^+ < K^+ < Cs^+$ under the same bulk concentration, and the rate of CO_2-to-CO conversion increases with the coverage increase of specifically adsorbed alkali metal cations.[46] Nevertheless, current investigations are mostly restricted to the interactions between cations and the reaction environment or intermediates in the CO_2RR, and the influence of cation-catalyst interaction on the CO_2RR performance has been almost neglected.

In this work, we report the fabrication of Cu nanosheet (CuNS) arrays on Cu foils by a two-step wet-chemical method. Significantly, the obtained CuNS arrays can promote the catalytic conversion of CO_2 to high-value C_{2+} products in 0.1 M $KHCO_3$, while the bare Cu foils mainly favor the generation of C_1 products under the same condition. Detailed studies show that the adsorption of K^+ ions on the surface of CuNSs is greatly enhanced compared with the pristine Cu foils. Density functional theory (DFT) calculations demonstrate that the CuNS shows intrinsic uneven electron distributions, which facilitates the adsorption of K^+ ions on the surface to optimize the surface electroactivity. The modified electronic structures of CuNSs lead to improved C-C coupling for C_{2+} products, while the bare Cu foils show strong preferences for the C_1 products.

RESULTS AND DISCUSSION

Synthesis and characterization of CuNS arrays

The CuNS arrays were prepared through a two-step method involving the surface oxidation treatment of Cu foils and the subsequent *in situ* electroreduction of CuO nanosheet (CuONS) arrays, as shown in Figure 1A (see more details in the experimental procedures below). Briefly, the pristine Cu foils were first immersed in an aqueous solution containing $K_2S_2O_8$ and NaOH at 60°C. After 30 min, the color of the Cu foils turned black, which indicates the formation of CuONSs on the surface of Cu foils. Then, the CuONSs were reduced to CuNSs at a given potential in the specific electrolyte for 10 min before the CO_2RR test, along with a color change from black to red.

The crystal structure of the Cu foil, the CuONS, and the CuNS was characterized by powder X-ray diffraction (XRD). As shown in Figure S1, the pristine Cu foil mainly

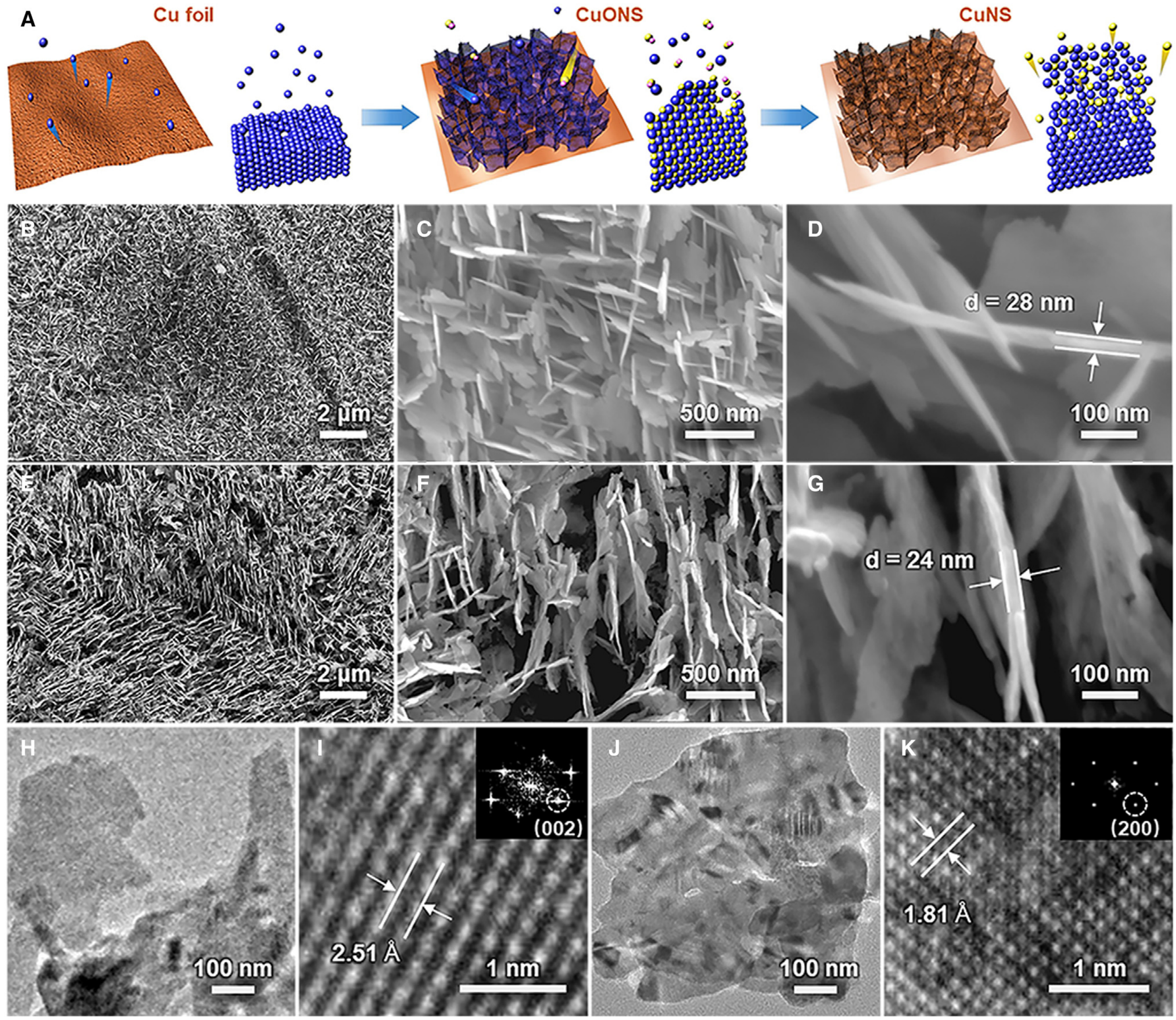

Figure 1. The synthesis and structural characterization of CuONS and CuNS-0.8

(A) A schematic illustration for the formation of CuNS from Cu foil.

(B–G) SEM images of CuONS (B–D) and CuNS-0.8 (E–G) at different magnification levels. The scale bars are 2 μm in (B) and (E), 500 nm in (C) and (F), and 100 nm in (D) and (G).

(H) TEM image of CuONS. The scale bar is 100 nm.

(I) HRTEM image of CuONS, with the corresponding fast Fourier transform (FFT) pattern as the inset. The scale bar is 1 nm.

(J) TEM image of CuNS-0.8. The scale bar is 100 nm.

(K) HRTEM image of CuNS-0.8, with the corresponding FFT pattern as the inset. The scale bar is 1 nm.

shows three peaks at 43.3°, 50.4°, and 74.1°, which correspond to the (111), (200), and (220) facets of Cu (PDF#04-0836), respectively. The peak at 50.4° is the dominant peak and has the strongest intensity, while the other peaks are almost neglectable, suggesting that the Cu foil is mostly (001) oriented (Figure S1B).[47] The CuONS demonstrates two sets of XRD peaks. Peaks located at 35.5° and 38.7° correspond to the (002) and (111) facets of CuO (PDF#45-0937) (Figure S1A). The peak at 50.4° is attributed to the (200) facet of the Cu substrate, implying that the CuONS is formed on the surface of the Cu foil and that the inner part of the Cu foil is not completely oxidized. After reduction, the obtained CuNS at the reduction potential of −0.8 V (vs. reversible hydrogen electrode [RHE], denoted as CuNS-0.8) shows a similar XRD pattern to the pristine Cu foil, indicating that the CuO is completely reduced to the metallic Cu. Besides, the chemical states of all the aforementioned materials were further verified by the X-ray photoelectron spectroscopy (XPS; Figure S2). For Cu foil, there are two peaks at 932.5 and 953.5 eV, and no satellite peaks can be found in the XPS spectrum, which matches well with the standard Cu spectrum (Figure S2A). For CuONSs, the strong satellite peaks between 940 and 945 eV are the typical characteristics corresponding to CuO (Figure S2B). The obtained CuNS shows a similar XPS spectrum to Cu foil along with very weak satellite peaks (Figure S2C), which are commonly believed to result from the oxidation of Cu nanostructures by air during the sample preparation. In addition, Raman spectroscopy was further used to evaluate the oxidation state of CuNSs prepared at the reduction potentials of −0.2, −0.5, −0.8, and −1.1 V (vs. RHE), as shown in Figure S3. Both CuNS-0.2 and CuNS-0.5 show a CuO peak at 628 cm^{-1} and two Cu_2O peaks at 218 and 146 cm^{-1}, while no obvious Cu_xO peaks can be observed on CuNS-0.8 and CuNS-1.1, indicating the complete reduction of CuONSs to metallic CuNSs.

Scanning electron microscopy (SEM), transmission electron microscopy (TEM), and high-resolution TEM (HRTEM) were combined to identify the morphology and structure of both CuONS and CuNS-0.8. As shown in Figures 1B and 1C, vertically aligned CuONS arrays are formed on the surface of the Cu foil after the oxidation step. The thickness of individual CuONSs is around 28 nm (Figure 1D). The typical SEM images of the CuNS-0.8 array are shown in Figures 1E and 1F. The thickness of individual CuNS-0.8 is about 24 nm, and the surface of individual nanosheets becomes uneven (Figure 1G). The nanosheet structure of CuONSs was also confirmed by TEM, as shown in Figure 1H. The HRTEM image in Figure 1I shows clear lattice fringes with an interplanar spacing of 2.51 Å, corresponding to the (002) facet of CuO.[48] The nanosheet structure of CuNSs can also be seen in Figure 1J, which displays an uneven surface. The HRTEM image of CuNS-0.8 shows lattice fringes with an interplanar spacing of 1.81 Å, which is attributed to the (200) facet of Cu (Figure 1K),[49,50] well consistent with the XRD result (Figure S1).

Electrochemical tests of CuNS arrays

The electrochemical tests were conducted in a gas-tight H-type cell under ambient conditions to study the electrochemical properties and CO_2RR performance of CuNS arrays. The cyclic voltammetry (CV) scan was adopted to identify the chemical states of CuNS-0.8 in 0.1 M $KHCO_3$ before the CO_2RR (Figure 2A). There are two typical reduction peaks at 0.48 and 0.18 V (vs. RHE) in the CV curve of CuONS arrays, which correspond to the reduction of Cu^{2+} to Cu^{+} and Cu^{+} to Cu, respectively. After the reduction of CuONS arrays at −0.8 V (vs. RHE) in 0.1 M $KHCO_3$ for 10 min, no reduction peaks can be found in the CV curve, indicating the pure metallic state of CuNS-0.8. This is well consistent with the XRD result (Figure S1). To further investigate the surface structure of the Cu foil and CuNS-0.8, the OH^- adsorption experiment and the electrochemically active surface area (ECSA) measurement were conducted in 1 M KOH (Figures 2B, 2C, and S4). As can be seen in Figure 2B, there are no obvious anodic or cathodic peaks in the CV curve of the Cu foil, suggesting that the Cu foil shows very weak specific adsorption of OH^-. While for the CuNS-0.8, the sharp and strong anodic and cathodic peaks at 0.35 and 0.33 V (vs. RHE), respectively, are attributed to the adsorption and desorption of OH^- on the Cu(100) facet, which reveals that the CuNS-0.8 is mainly enclosed by the {100} facet,[51,52] agreeing well with the HRTEM result (Figure 1K). In addition, the double-layer capacitances of CuNS-0.8 and Cu foil were measured to be 1.67 and 0.56 mF/cm^2, which indicates

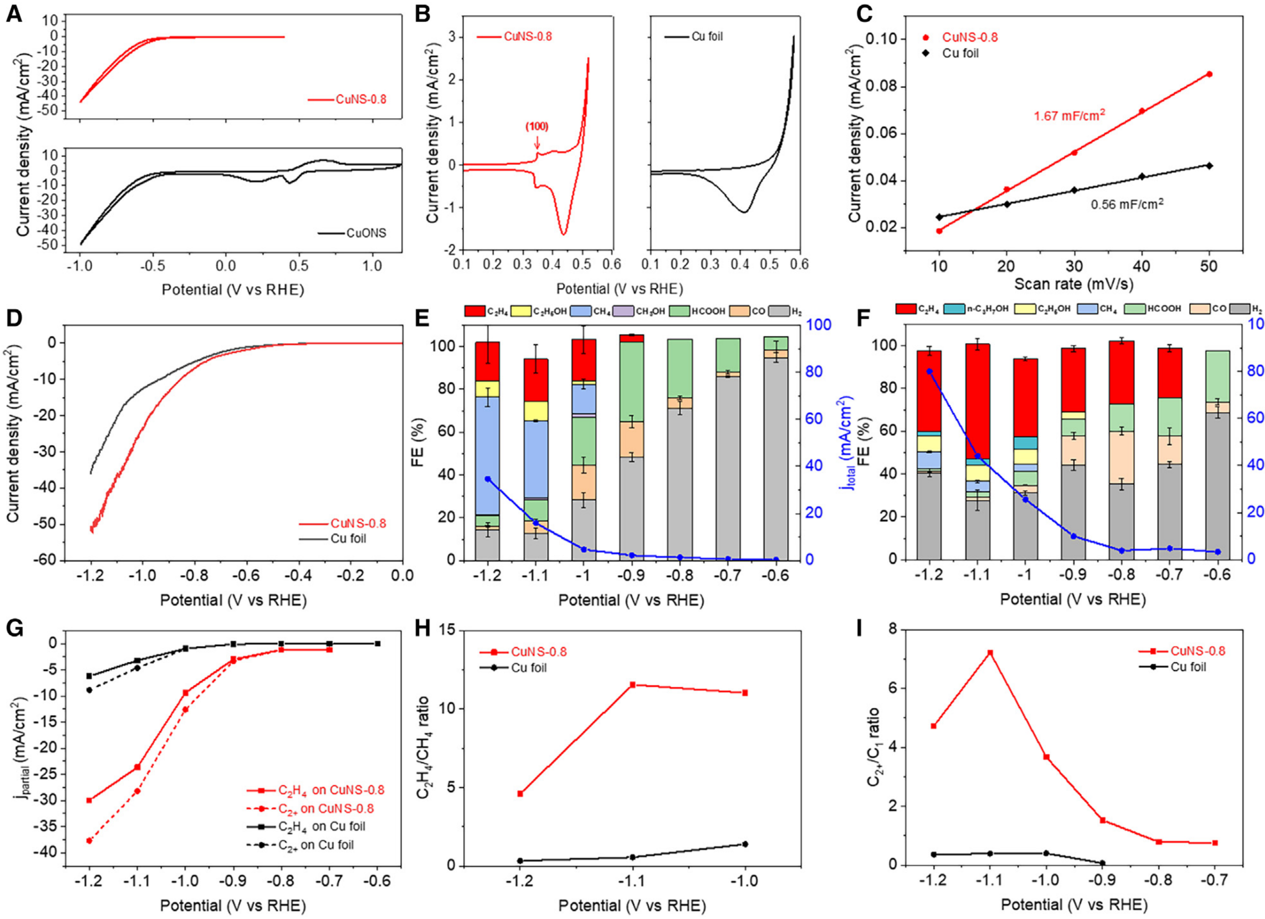

Figure 2. The electrochemical properties and performance of Cu foil and CuNS-0.8

(A) CV curves of CuNS after reducing the CuONS at −0.8 V (vs. RHE).

(B) The OH^- adsorption profiles of CuNS-0.8 (left panel) and Cu foil (right panel).

(C) The charging current density differences plotted against the scan rates over CuNS-0.8 and Cu foil.

(D) LSV curves of CuNS-0.8 and Cu foil in CO_2-saturated 0.1 M $KHCO_3$ with a scan rate of 10 mV/s.

(E and F) The product distributions and current densities of (E) Cu foil and (F) CuNS-0.8 at different potentials. The error bars represent the standard deviation around the mean of 3 measurements.

(G) The partial current densities of C_2H_4 and C_{2+} products on CuNS-0.8 and Cu foil at different potentials.

(H) The ratio of C_2H_4 to CH_4 on CuNS-0.8 and Cu foil at different potentials.

(I) The ratio of C_{2+} products to C_1 products on CuNS-0.8 and Cu foil at different potentials.

that the ECSA of CuNS-0.8 is almost 3 times that of the Cu foil,[53] as shown in Figure 2C.

The CO_2RR performance of Cu foils and CuNS-0.8 was firstly evaluated in 0.1 M $KHCO_3$. The linear sweep voltammetry (LSV) curves show that CuNS-0.8 has a higher current density than the Cu foils, which might result from the higher ECSA of CuNS-0.8 (Figure 2D). Figure 2E shows the product distribution of Cu foils. Specifically, at the potentials from −0.6 to −0.8 V (vs. RHE), the major gaseous products are H_2 and CO, and the liquid product is HCOOH. The C_2H_4 can be detected at −0.9 V (vs. RHE) with an FE of 3.3%. The maximum FE_{C2H4} and FE_{C2+} are 19.9% and 28.8% on the Cu foil, respectively. As the applied potential shifts to more negative values, CH_4 gradually becomes the dominant CO_2-reduction product, and the FE_{CH4} reaches 54.8% at −1.2 V (vs. RHE). In sharp contrast, CuNS-0.8 shows a very different product distribution from the Cu foil (Figure 2F). Specifically, at −0.6 V (vs. RHE), the detected products are H_2, HCOOH, and CO, which are similar to the Cu foil. Notably, C_2H_4 can be detected at −0.7 V (vs. RHE) and becomes the major product as the applied potential changes to more negative values. The FE_{C2H4} shows a volcano trend, which first increases to the maximum value of 53.6% at −1.1 V (vs. RHE) and then decreases. The typical liquid products at this potential are $HCOO^-$, C_2H_5OH, n-C_3H_7OH, and a very trace amount of acetate (Figures S5 and S6). And the FE of C_{2+} products also reaches a maximum value of 64% at −1.1 V (vs. RHE). Note that the FE of CH_4 on CuNS-0.8 is below 10%, implying that the production of CH_4 is greatly suppressed compared with the Cu foil. The CuNS-0.8 also demonstrates a much larger current density than the Cu foil in the tested potential window (Figures 2E and 2F). The partial current densities of both C_2H_4 and C_{2+} products on CuNS-0.8 are much higher than those of Cu foils (Figure 2G). At −1.1 V (vs. RHE), the partial current densities of C_2H_4 and C_{2+} products on CuNS-0.8 are −23.6 and −28.2 mA/cm^2, respectively, which are 7.4 and 6.1 times those of Cu foils. At −1.1 V (vs. RHE), the C_2H_4/CH_4 ratio on CuNS-0.8 is 11.5, while it is only 0.6 on Cu foils (Figure 2H). Significantly, the ratio of C_{2+} to C_1 products (C_{2+}/C_1) on CuNS-0.8 is as high as 7.2 at −1.1 V (vs. RHE), which is 18 times that on Cu foils (Figure 2I).

The stability of CuNS-0.8 was also evaluated at −1.1 V (vs. RHE). As shown in Figure S7, the selectivity of CuNS-0.8 toward C_2H_4 production can be well maintained above 50% in the first 1 h (Figure S8A). After about 1.5 h, the FE_{C2H4} decreases to around 35% and keeps this level in the following 3.5 h. In the early stage, the nanosheet array structure can be well preserved (Figures S8A and S8B), so it shows a relatively high FE_{C2H4}. However, when the electrolysis continued for a long time, the nanosheet array structure of CuNS-0.8 collapsed (Figure S8C), resulting in the change of their surface structure and the corresponding sharp decrease of FE_{C2H4}. These results further indicate that the nanosheet structure plays a vital role in promoting the selective formation of C_{2+} products. Besides, it should be mentioned that the CO_2RR performance of CuNSs has been optimized by systematically tuning the reduction potentials of CuONS from −0.2 to −1.1 V (vs. RHE), as shown in Figures 2F and S9–S12.

The sharp difference in CO_2RR selectivity of CuNS-0.8 and Cu foils is attributed to the uneven nanosheet structure of CuNS-0.8 as well as the cation-catalyst interaction effect. On the one hand, uneven two-dimensional nanosheets can lead to electron perturbation and change in the electronic structure of surface atoms.[54] On the other hand, cations are essential to initiate the CO_2RR, as mainly the HER occurs in the absence of cations.[55] The modified electron distribution of uneven nanosheets could affect the specific adsorption of cations and thus modulate the CO_2RR performance.[40,56,57] To validate this hypothesis, the density of K^+ ions adsorbed on both CuNS-0.8 and Cu foil was measured at −1.1 V (vs. RHE). As shown in Figure 3A, the densities of adsorbed K^+ ions on CuNS-0.8 are as high as 11.69 and 3.92 μmol/cm^2 based on the geometric area and ECSA, respectively, while the values are only 0.80 μmol/cm^2 on Cu foils. These observations suggest that the cation-catalyst interaction on CuNS-0.8 has been significantly enhanced compared with the Cu foil.

To further investigate the cation-catalyst interaction effects, we have also evaluated the CO_2RR performance of CuNS-0.8 in 0.1 M $LiHCO_3$, 0.1 M $NaHCO_3$, and 0.1 M $CsHCO_3$ (Figures 3B–3D). Three independent CuNS-0.8 electrodes were adopted, and their ECSA profiles are shown in Figure S13. In 0.1 M $LiHCO_3$, H_2 is the dominant product at all tested potentials (Figure 3B). At low applied potentials, CO and HCOOH are the dominant CO_2-reduction products. At high applied potentials

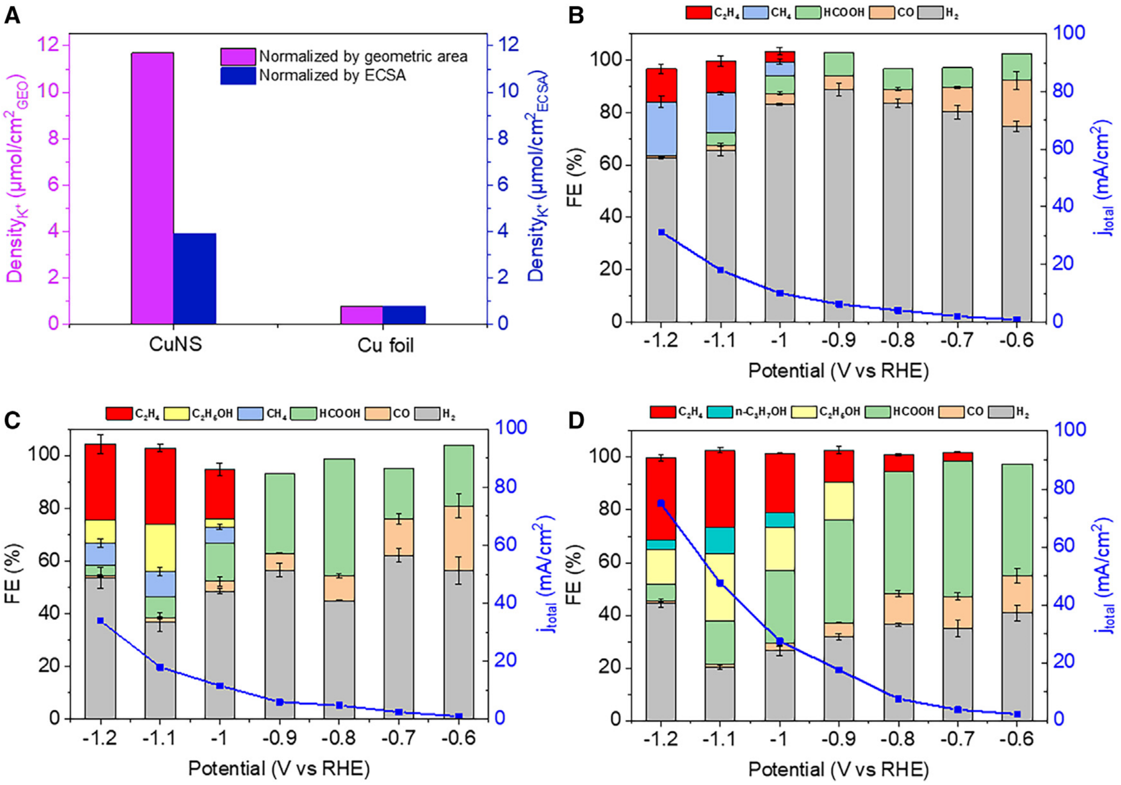

Figure 3. The cation-catalyst interaction effects on the CO_2RR performance of CuNS-0.8

(A) The density of K^+ ions adsorbed on CuNS-0.8 and Cu foil.

(B–D) The CO_2RR performance of CuNS-0.8 in CO_2-saturated (B) 0.1 M $LiHCO_3$, (C) 0.1 M $NaHCO_3$, and (D) 0.1 M $CsHCO_3$. The error bars represent the standard deviation around the mean of 3 measurements.

(i.e., from −1 to −1.2 V [vs. RHE]), CH_4 gradually becomes the major CO_2-reduction product. The maximum FE_{C2H4} is merely 12.7% at −1.2 V (vs. RHE), which accounts for the whole part of C_{2+} products. In 0.1 M $NaHCO_3$, the production of C_2H_4 and C_2H_5OH is greatly enhanced between −1 and −1.2 V (vs. RHE), as can be seen in Figure 3C. The maximum FE_{C2H4} and FE_{C2+} are 28.9% and 46.7% at −1.1 V (vs. RHE), respectively. In 0.1 M $KHCO_3$, the production of C_2H_4 is further enhanced, with a maximum FE_{C2H4} of 53.6% and a maximum FE_{C2+} of 64% at −1.1 V (vs. RHE), as discussed before (Figure 2F). In 0.1 M $CsHCO_3$, C_2H_4 can also be detected at the low potential of −0.7 V (vs. RHE), and the maximum FE_{C2H4} is 29.2% at −1.1 V (vs. RHE), as shown in Figure 3D. Although the FE_{C2H4} is lower than that in 0.1 M $KHCO_3$, the production of alcohols (including C_2H_5OH and n-C_3H_7OH) is significantly boosted, with a high FE of 35.5%. The maximum FE_{C2+} is 64.7% in 0.1 M $CsHCO_3$ at −1.1 V (vs. RHE), which is almost equal to that in 0.1 M $KHCO_3$. Notably, both the FE_{C2H4} of CuNS-0.8 in 0.1 M $KHCO_3$ and the $FE_{alcohols}$ of CuNS-0.8 in 0.1 M $CsHCO_3$ are much higher than most of the previously reported Cu-based catalysts (Table S1). As the cations of the electrolyte change from Li^+ to Cs^+, the CuNS-0.8 shows a volcano trend in FE_{C2H4} and a sharp increase in the selectivity of C_{2+} alcohols, suggesting that the catalytic selectivity of CuNS-0.8 is closely related to the cations. According to the previous studies, the cations with larger crystal radii demonstrate smaller hydrated radii and thus show higher densities on the surface of the electrode,[51] which indicates that the density of alkali cations specifically adsorbed on Cu should follow the order of $Li^+ < Na^+ < K^+ < Cs^+$.[35] Bearing this in mind, it is anticipated that Li^+ and Na^+ can only modulate the electronic structure of CuNSs

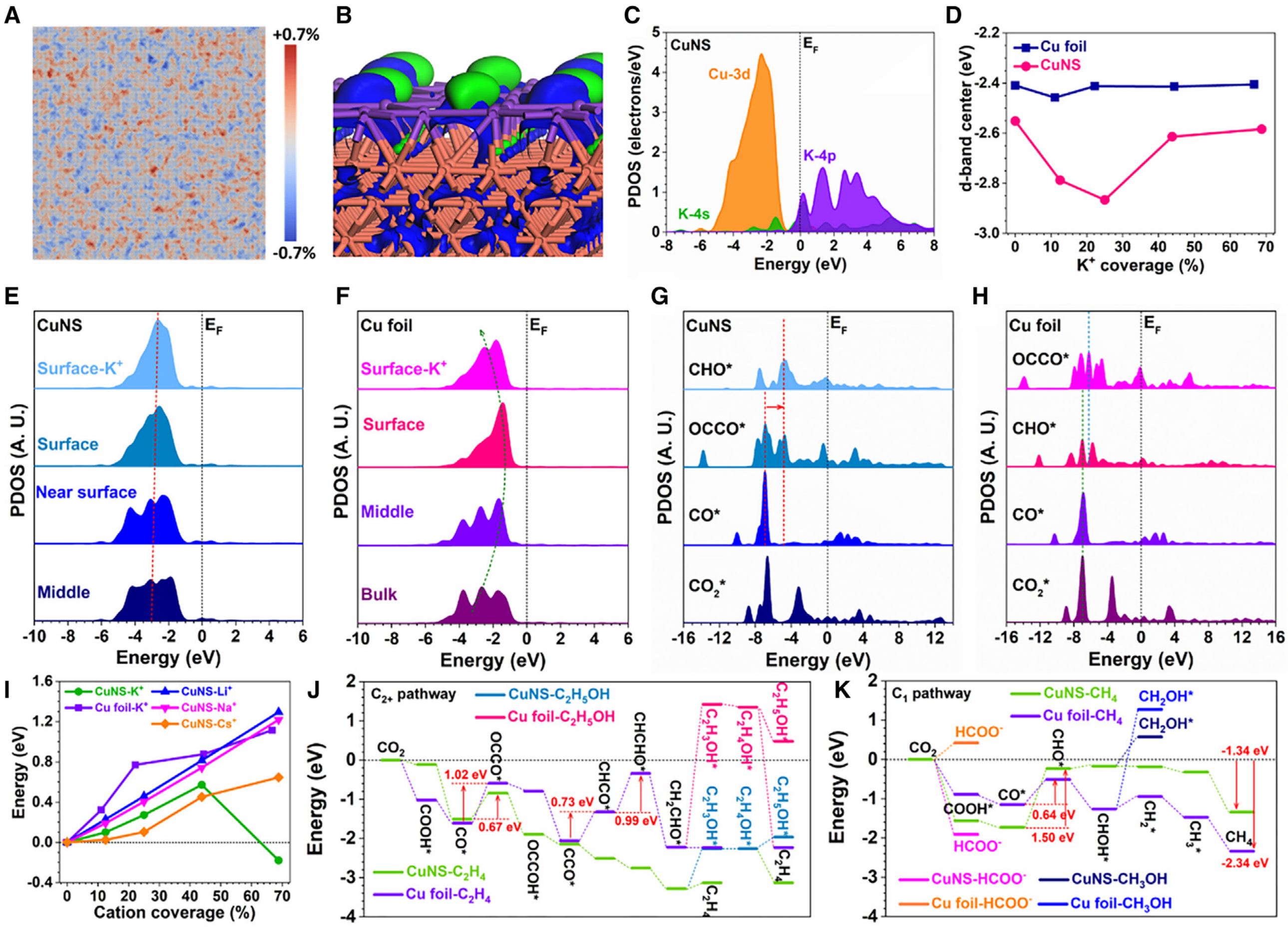

Figure 4. Theoretical calculations with the CuNS and Cu foil for CO_2RR

(A) The atomic strain distributions of CuNS.

(B) The electronic distributions of bonding and anti-bonding orbitals near the Fermi level (E_F) of CuNS with K^+ ions on the surface. Brown ball, Cu; purple ball, K^+; blue isosurface, bonding orbitals; green isosurface, anti-bonding orbitals.

(C) The PDOSs of CuNS with adsorption of K^+ ions.

(D) The dependence of the d-band center on the K^+ ion coverage.

(E and F) The site-dependent PDOS of Cu-3d in (E) CuNS and (F) Cu foil.

(G and H) The PDOS of key adsorbates of CO_2RR for C_1 and C_2 products in (G) CuNS and (H) Cu foil.

(I) The adsorption energies of different alkali cations on CuNS and Cu foil.

(J and K) The reaction energies of (J) C_{2+} and (K) C_1 pathways of CO_2RR on CuNS and Cu foil, respectively.

to a slight degree because of their relatively lower densities on the surface of the catalyst, while K^+ and Cs^+ can tune the electronic structure of CuNSs to a larger degree and thereby greatly improve the selectivity of C_{2+} products.

Theoretical calculations

We have further introduced theoretical calculations to study the CO_2RR performance of CuNS-0.8. Due to the ultrathin thickness, the CuNS shows evident atomic strain without even distributions in the range from −0.7% to 0.7% (Figure 4A). This leads to the intrinsically uneven electronic distributions of the CuNS, which is more likely to bind with the K^+ ions in the electrolyte and further modify the surface electronic structures. Notably, after the adsorption of K^+ ions on the surface, the surface electronic structures are strongly perturbed (Figure 4B). The electron-rich surfaces are able to guarantee a highly efficient electron transfer from CuNSs to the intermediates for deep reduction of CO_2 toward C_{2+} products. Detailed electronic structures of CuNSs have been demonstrated through the partial density of states (PDOSs), as shown in Figure 4C. Importantly, Cu-3d shows a dominant peak at E_V-2.30 eV (E_V = 0 eV), while the s and p orbitals of surface K^+ ions mostly locate above the E_F. It is noted that K-4s orbitals overlap with the Cu-3d orbitals, which alleviates the electron transfer barrier. The d-band center in the Cu foil is overall higher than that of the CuNS, which potentially results in the overbinding of the CO* and causes the transition to CHO* and C_1 products (Figure 4D). As the K^+ ion coverage increases, the electronic structures in both CuNSs and Cu foil are affected in a similar trend, where the sensitivity in CuNSs is much stronger than that of Cu foil. This indicates that K^+ ions more actively interact with the CuNS surface, which induces the strong electric field to modulate surface electronic structures and benefit the stabilization of key intermediates toward the C_{2+} products. Within the CuNS, the Cu-3d orbitals display a relatively stable electronic structure with a subtle upshifting trend (Figure 4E). The appropriate d-band center of Cu-3d orbitals ensures the suitable binding strength of CO*, which promotes the C-C couplings for C_{2+} reaction pathways. Meanwhile, the Cu-3d orbitals in Cu foil show an evident upshifting from the bulk to the surface (Figure 4F). The K^+ ion coverage on the surface shows a downshifting trend of the Cu-3d, supporting that the electrolyte cations modulate the surface electroactivity. Due to the stronger binding trends with key intermediates toward the C_{2+} products induced by the surface cation effects, the CuNS shows much higher C_{2+} selectivity than that of the Cu foil. For the selectivity of the C_1 or C_{2+} pathways, the PDOS of the key adsorbates on the CuNS demonstrates that the conversion from CO_2* to OCCO* shows much smooth electron transfer, while the formation of CHO* shows an evident deviation (Figure 4G). This supports that the formation of C_1 products meets higher energy barriers than that of the C_{2+} products. The Cu foil shows an opposite trend (Figure 4H). Note that the formation of CHO* shows a linear correlation, while the C-C couplings exhibit deviation from the correlation, leading to a strong preference for the C_1 pathways.

As a comparison, the adsorption of other alkali cations (Li^+, Na^+, and Cs^+) was also investigated together with K^+ (Figure 4I). Li^+ has shown the highest adsorption energies due to its lightest weight, which is difficult to be stabilized. Remarkably, at the lower coverage, Cs^+ has displayed a stronger adsorption preference than other alkali cations, which is attributed to the much larger atomic mass and smaller hydrated radius. However, the adsorption energies of K^+ on the CuNS surface show a sudden drop and display negative binding energy at high coverage, leading to a strong preference for higher coverage (Figure 3A). In contrast, the Cu foil shows even higher binding energies than CuNSs with a continuously increasing trend as K^+ ion coverage increases, supporting the low possibility of adsorption (Figure 3A). The coverage trends of different alkali cations are well consistent with the corresponding CO_2RR performances (Figures 2F and 3B–3D).

For the C_{2+} reaction pathways, the CuNS displays a much smaller energy barrier for the C-C couplings and less energy barriers than that of the Cu foil toward the formation of C_2H_4 (Figure 4J). In addition, the formation of CH_3CH_2OH delivers a high energy barrier of 1.02 eV, supporting the low FE in experiments (Figure 2F). For the formation of C_2H_4, the conversion from CH_2CHO is more preferred over the CH_2CH_2OH due to lower energy barriers. For the C_1 pathways, the formation of $HCOO^-$ and CO is more favored for CuNS and Cu foil, respectively (Figure 4K). For the CH_4 pathway, the formation of CHO* shows an energy barrier of 1.50 and 0.64 eV for CuNSs and Cu foil, respectively. The much higher energy barrier of the

C_1 pathways and stronger reaction trend of the C_{2+} pathways lead to the higher selectivity of C_{2+} products on CuNSs, agreeing well with experimental observation (Figure 2F). In the meantime, the formation of CH_4 is also favored for the Cu foil due to the much lower energy barriers than the C_{2+} pathways (Figure 2E). For both CuNSs and Cu foil, the formation of CH_3OH is not preferred, which is well consistent with the experimental results (Figures 2E and 2F).

In summary, we have successfully prepared a self-supported CuNS array electrode with an uneven surface. Compared with the bare Cu foil, the CuNS demonstrated remarkably enhanced selectivity toward C_{2+} products in the CO_2RR. At −1.1 V (vs. RHE), a maximum FE of C_{2+} products of 64% was achieved on CuNSs in 0.1 M $KHCO_3$, which is over two times that on the Cu foil. Detailed studies revealed that the adsorption of K^+ ions on the surface of CuNSs is significantly enhanced compared with the Cu foil. DFT calculations have revealed that the high selectivity toward the C_{2+} reaction pathway of the CuNS is attributed to the energetically favored K^+ adsorption on the surface, which not only modifies the electronic structures of Cu sites but also promotes the C-C couplings. The CuNS displays much lower energy barriers and higher reaction trends for the generation of C_{2+} products. It is believed that this work will open up new opportunities for boosting the CO_2RR performance via rationally tuning the cation-catalyst interaction.

EXPERIMENTAL PROCEDURES

Resource availability

Lead contact

Further information and requests for resources should be directed to and will be fulfilled by the lead contact, Zhanxi Fan (zhanxi.fan@cityu.edu.hk).

Materials availability

This study did not generate new unique reagents. All of the chemicals, materials, and experimental procedures have been provided.

Data and code availability

All data generated during this study are available from the lead contact upon reasonable request. The study did not generate unique code.

Chemicals and materials

The Cu foil (99.9%, 0.125 mm in thickness) was purchased from Alfa Aesar. $K_2S_2O_8$ (99.5%) and NaOH (95%) were purchased from Macklin. Acetone (98%), HCl (37%), $LiHCO_3$ (99.99%), $NaHCO_3$ (99.99%), $KHCO_3$ (99.99%), $CsHCO_3$ (99.99%), D_2O, and dimethyl sulfoxide (DMSO) were purchased from Aladdin. All chemical reagents were used as received without further purification. The CO_2 gas (99.999%) was purchased from South China Special Gas.

Electrode preparation

The CuNS array was prepared by *in situ* electroreduction of CuONS. Firstly, the CuONS was obtained by a chemical oxidation method. In specific, a large piece of Cu foil was cut into small pieces with a size of 1 × 0.5 cm, followed by washing with 3 M HCl, acetone and de-ionized water (18.2 MΩ) sequentially under sonication to remove the impurities. In parallel, 0.7 g $K_2S_2O_8$ and 2.7 g NaOH were dissolved into 50 mL de-ionized water (18.2 MΩ). The obtained solution was transferred into a 100 mL beaker and heated to 60°C. Then, the Cu foils were immersed in the aforementioned solution and maintained for 30 min. The color of the Cu foils turned from yellow to black, which indicates the formation of CuONSs. After that, the resultant samples were collected and rinsed with ethanol and water 5 times and later dried at 60°C in a vacuum oven overnight. Finally, the CuNS electrodes were obtained by *in situ* reducing the CuONSs at a given potential.

Characterizations

SEM measurements of all samples were conducted on a QUATTRO S scanning electron microscope. XRD analysis was performed on Rigaku SmartLab SE X-ray powder diffractometer with Cu-K_α radiation. XPS spectra were obtained on an ESCALAB-MKII spectrometer with an Al K_α X-ray source using C 1s (284.5 eV) as the reference. The TEM images and HRTEM images were collected on a JEOL JEM-2100F transmission electron microscope.

Electrochemical CO_2RR test

The electrochemical CO_2RR measurements were conducted in a gas-tight H-type cell (Gaoss Union), which is separated by an ion exchange membrane (Nafion 117, Dupont). The 0.1 M $KHCO_3$ aqueous solution was used as the electrolyte and was saturated by CO_2 before the electrochemical test. During the CO_2RR, CO_2 gas was purged into the cathodic chamber at a rate of 30 standard cubic centimeters per minute (sccm), and the electrolyte in the cathodic chamber was stirred at 400 RPM. The electrochemical measurements were carried out on a CHI 760E workstation. The platinum mesh and Ag/AgCl (saturated with KCl) were used as the counter electrode and reference electrode, respectively. The obtained CuNSs served as the working electrode, which was prepared via the *in situ* electroreduction of the CuONS before the CO_2RR test. During the electrolysis test, the chronoamperometry measurement was adopted. At each potential, the time of electrolysis was 45 min so as to accumulate an adequate amount of liquid products for quantification analysis. All potentials were compensated and converted to RHE scale with ohmic compensation according to Equation 1:

$$E\ (\text{vs. RHE}) = E\ (\text{vs. Ag/AgCl}) + 0.197 + 0.0591 \times \text{pH} + 0.8 \times iR. \qquad \text{(Equation 1)}$$

All gas products were quantified by an online gas chromatograph (GC; Agilent 7890B). The GC system is equipped with three channels. One channel is equipped with a thermal conductivity detector (TCD) to quantify H_2. Another channel is equipped with a methanator and a flame ionization detector (FID) to analyze CO. And the third channel is equipped with another FID to analyze other gas products, such as CH_4, C_2H_4, and C_2H_6. Liquid products were quantified by a nuclear magnetic resonance (NMR) spectroscopy (300 MHz, Bruker AVANCE III BBO Probe). After getting the liquid sample, a 600 μL aliquot of the electrolyte was mixed with 30 μL D_2O and 16.7 ppm (m/m) DMSO as the internal standard. The ^1H spectrum was acquired with water suppression using a pre-saturation method.

K^+ density measurement

The density of K^+ was determined by using inductively coupled plasma optical emission spectrometry (ICP-OES; Optima 8000). After getting the Cu foil and CuNS-0.8, the electrodes were set in the same electrolysis system as the CO_2RR. The potential was set at −1.1 V (vs. RHE) and held for 120 s. Then, the electrode was carefully pulled out of the electrolyte, followed by the careful rinsing with 5 mL de-ionized water. After that, the density of K^+ in the water was tested by ICP-OES.

FE calculation

The FE of gas and liquid products was calculated based on Equations 2 and 3,

$$FE_{gas} = \frac{C_{gas} \times v \times z \times F}{i_{total} \times 22,400} \times 100\% \quad \text{(Equation 2)}$$

$$FE_{liquid} = \frac{C_{liquid} \times V \times z \times F}{Q} \times 100\% \quad \text{(Equation 3)}$$

where C_{gas} (ppm) is the volume concentration of gas products read from the GC; υ (sccm) is the flow rate of CO_2; z is the number of charges transferred when forming one molecule of the products; F is the Faradaic constant (96,485C/mol); i_{total} (mA) is the measured current read from the electrochemical workstation; 22,400 is the molar volume of gas at standard conditions (mL/mol); C_{liquid} (mol/L) is the concentration of liquid products obtained from NMR measurement according to the calibration curves (Figure S14); V is the amount of electrolyte in the cathode chamber (8 mL); and Q (C) is the total amount of charges passed through the electrode, which can be read from the electrochemical workstation.

The partial current density ($j_{partial}$) of the products was calculated by Equation 4,

$$j_{partial} = j_{total} \times FE \quad \text{(Equation 4)}$$

where j_{total} is the total geometric current density.

Calculation setup

To investigate the CO_2RR performance of CuNSs and Cu foil, we have introduced the DFT calculations within the CASTEP packages.[58] For the functionals, the generalized gradient approximation (GGA) and Perdew-Burke-Ernzerhof (PBE) were both chosen to achieve accurate descriptions of exchange-correlation interactions.[59–61] Meanwhile, we have applied the ultrasoft pseudopotentials for all the geometry optimizations and set the plane-wave basis cutoff energy to 380 eV. In addition, the Broyden-Fletcher-Goldfarb-Shannon (BFGS) algorithm[62] was selected with the coarse quality setting of k-points for all energy minimizations in this work. For both CuNSs and Cu foil, the (100) surfaces were chosen according to the experimental characterizations with 20 Å vacuum space introduced in the z axis to guarantee the geometry relaxations. The following convergence criteria were applied: the Hellmann-Feynman forces, the total energy difference, and the interionic displacement should not exceed 0.001 eV/Å, 5×10^{-5} eV/atom, and 0.005 Å, respectively.

SUPPLEMENTAL INFORMATION

Supplemental information can be found online at https://doi.org/10.1016/j.xcrp.2023.101366.

ACKNOWLEDGMENTS

This work was supported by grants (project nos. JCYJ20220530140815035 and JCYJ20220531090807017) from the Shenzhen Science and Technology Program; grants (project nos. 22005258 and 22175148) from the National Natural Science Foundation of China; a grant (project no. 21309322) from the Research Grants Council of Hong Kong, the National Natural Science Foundation of China/Research Grant Council of Hong Kong Joint Research Scheme (N_PolyU502/21), and ITC via Hong Kong Branch of National Precious Metals Material Engineering Research Center (NPMM); funding for the Projects of Strategic Importance of The Hong Kong Polytechnic University (project code: 1-ZE2V); grants (project nos. 9610480, 7005600, and 9680301) from the City University of Hong Kong; and by the Departmental General Research Fund (project code: ZVUL) from the Department of Applied Biology and Chemical Technology of the Hong Kong Polytechnic University. B.H. is also thankful for the support of the Research Center for Carbon-Strategic Catalysis (RC-CSC), the Research Institute for Smart Energy (RISE), and the Research Institute for Intelligent Wearable Systems (RI-IWEAR) of the Hong Kong Polytechnic University.

AUTHOR CONTRIBUTIONS

J.Y., M.S., J.W., Y.W., and Y.L. contributed equally to this work. Z.F. supervised the research. Z.F., J.Y., J.W., Y.W., and Y.L. designed and performed most of the experiments and data analysis. M.S. and B.H. performed the DFT simulations. J.Y., M.S., B.H., and Z.F. co-wrote the manuscript. P.L., Y.M., J.Z., W.C., X.Z., and C.-S.L. assisted with the experiments, characterizations, and visualization. All authors discussed the results and assisted during manuscript preparation.

DECLARATION OF INTERESTS

The authors declare no competing interests.

Received: December 13, 2022
Revised: February 19, 2023
Accepted: March 13, 2023
Published: April 7, 2023

REFERENCES

1. Witze, A. (2022). Extreme heatwaves: surprising lessons from the record warmth. Nature *608*, 464–465. https://doi.org/10.1038/d41586-022-02114-y.
2. Kibria, M.G., Edwards, J.P., Gabardo, C.M., Dinh, C.T., Seifitokaldani, A., Sinton, D., and Sargent, E.H. (2019). Electrochemical CO_2 reduction into chemical feedstocks: from mechanistic electrocatalysis models to system design. Adv. Mater. *31*, 1807166. https://doi.org/10.1002/adma.201807166.
3. Wang, Y., Zhou, J., Lin, C., Chen, B., Guan, Z., Ebrahim, A.M., Qian, G., Ye, C., Chen, L., Ge, Y., et al. (2022). Decreasing the overpotential of aprotic Li-CO_2 batteries with the in-plane alloy structure in ultrathin 2D Ru-based nanosheets. Adv. Funct. Mater. *32*, 2202737. https://doi.org/10.1002/adfm.202202737.
4. Zhou, J., Wang, T., Chen, L., Liao, L., Wang, Y., Xi, S., Chen, B., Lin, T., Zhang, Q., Ye, C., et al. (2022). Boosting the reaction kinetics in aprotic lithium-carbon dioxide batteries with unconventional phase metal nanomaterials. Proc. Natl. Acad. Sci. USA *119*, 2204666119. https://doi.org/10.1073/pnas.2204666119.
5. Fan, Z., Bosman, M., Huang, Z., Chen, Y., Ling, C., Wu, L., Akimov, Y.A., Laskowski, R., Chen, B., Ercius, P., et al. (2020). Heterophase fcc-2H-fcc gold nanorods. Nat. Commun. *11*, 3293. https://doi.org/10.1038/s41467-020-17068-w.
6. Zhu, Y., Cui, X., Liu, H., Guo, Z., Dang, Y., Fan, Z., Zhang, Z., and Hu, W. (2021). Tandem catalysis in electrochemical CO_2 reduction reaction. Nano Res. *14*, 4471–4486. https://doi.org/10.1007/s12274-021-3448-2.
7. Ješić, D., Lašič Jurković, D., Pohar, A., Suhadolnik, L., and Likozar, B. (2021). Engineering photocatalytic and photoelectrocatalytic CO_2 reduction reactions: mechanisms, intrinsic kinetics, mass transfer resistances, reactors and multi-scale modelling simulations. Chem. Eng. J. *407*, 126799. https://doi.org/10.1016/j.cej.2020.126799.
8. Kovačič, Ž., Likozar, B., and Huš, M. (2020). Photocatalytic CO_2 reduction: a review of Ab initio mechanism, kinetics, and multiscale modeling simulations. ACS Catal. *10*, 14984–15007. https://doi.org/10.1021/acscatal.0c02557.
9. Ge, L., Rabiee, H., Li, M., Subramanian, S., Zheng, Y., Lee, J.H., Burdyny, T., and Wang, H. (2022). Electrochemical CO_2 reduction in membrane-electrode assemblies. Chem *8*, 663–692. https://doi.org/10.1016/j.chempr.2021.12.002.
10. De Luna, P., Hahn, C., Higgins, D., Jaffer, S.A., Jaramillo, T.F., and Sargent, E.H. (2019). What would it take for renewably powered electrosynthesis to displace petrochemical processes? Science *364*, eaav3506. https://doi.org/10.1126/science.aav3506.
11. Masel, R.I., Liu, Z., Yang, H., Kaczur, J.J., Carrillo, D., Ren, S., Salvatore, D., and Berlinguette, C.P. (2021). An industrial perspective on catalysts for low-temperature CO_2 electrolysis. Nat. Nanotechnol. *16*, 118–128. https://doi.org/10.1038/s41565-020-00823-x.
12. Lees, E.W., Mowbray, B.A.W., Parlane, F.G.L., and Berlinguette, C.P. (2021). Gas diffusion electrodes and membranes for CO_2 reduction electrolysers. Nat. Rev. Mater. *7*, 55–64. https://doi.org/10.1038/s41578-021-00356-2.
13. Yu, J., Wang, J., Ma, Y., Zhou, J., Wang, Y., Lu, P., Yin, J., Ye, R., Zhu, Z., and Fan, Z. (2021). Recent progresses in electrochemical carbon dioxide reduction on copper-based catalysts toward multicarbon products. Adv. Funct. Mater. *31*, 2102151. https://doi.org/10.1002/adfm.202102151.
14. Wang, J., Zhang, Y., Ma, Y., Yin, J., Wang, Y., and Fan, Z. (2022). Electrocatalytic reduction of carbon dioxide to high-value multicarbon products with metal–organic frameworks and their derived materials. ACS Mater. Lett. *4*, 2058–2079. https://doi.org/10.1021/acsmaterialslett.2c00751.
15. Xiao, C., and Zhang, J. (2021). Architectural design for enhanced C_2 product selectivity in electrochemical CO_2 reduction using Cu-based catalysts: a review. ACS Nano *15*, 7975–8000. https://doi.org/10.1021/acsnano.0c10697.
16. Guo, W., Zhang, Y., Su, J., Song, Y., Huang, L., Cheng, L., Cao, X., Dou, Y., Ma, Y., Ma, C., et al. (2022). Transient solid-state laser activation of indium for high-performance reduction of CO_2 to formate. Small *18*, 2201311. https://doi.org/10.1002/smll.202201311.
17. Su, X., Jiang, Z., Zhou, J., Liu, H., Zhou, D., Shang, H., Ni, X., Peng, Z., Yang, F., Chen, W., et al. (2022). Complementary operando spectroscopy identification of in-situ generated metastable charge-asymmetry Cu_2-CuN_3 clusters for CO_2 reduction to ethanol. Nat. Commun. *13*, 1322. https://doi.org/10.1038/s41467-022-29035-8.
18. Ma, Y., Wang, J., Yu, J., Zhou, J., Zhou, X., Li, H., He, Z., Long, H., Wang, Y., Lu, P., et al. (2021). Surface modification of metal materials for high-performance electrocatalytic carbon dioxide reduction. Matter *4*, 888–926. https://doi.org/10.1016/j.matt.2021.01.007.

19. Ma, Y., Yu, J., Sun, M., Chen, B., Zhou, X., Ye, C., Guan, Z., Guo, W., Wang, G., Lu, S., et al. (2022). Confined growth of silver-copper Janus nanostructures with {100} facets for highly selective tandem electrocatalytic carbon dioxide reduction. Adv. Mater. *34*, 2110607. https://doi.org/10.1002/adma.202110607.

20. Wang, J., Yu, J., Sun, M., Liao, L., Zhang, Q., Zhai, L., Zhou, X., Li, L., Wang, G., Meng, F., et al. (2022). Surface molecular functionalization of unusual phase metal nanomaterials for highly efficient electrochemical carbon dioxide reduction under industry-relevant current density. Small *18*, 2106766. https://doi.org/10.1002/smll.202106766.

21. Chen, Y., Fan, Z., Wang, J., Ling, C., Niu, W., Huang, Z., Liu, G., Chen, B., Lai, Z., Liu, X., et al. (2020). Ethylene selectivity in electrocatalytic CO_2 reduction on Cu nanomaterials: a crystal phase-dependent study. J. Am. Chem. Soc. *142*, 12760–12766. https://doi.org/10.1021/jacs.0c04981.

22. Yang, P.P., Zhang, X.L., Gao, F.Y., Zheng, Y.R., Niu, Z.Z., Yu, X., Liu, R., Wu, Z.Z., Qin, S., Chi, L.P., et al. (2020). Protecting copper oxidation state via intermediate confinement for selective CO_2 electroreduction to C_{2+} fuels. J. Am. Chem. Soc. *142*, 6400–6408. https://doi.org/10.1021/jacs.0c01699.

23. Liu, W., Zhai, P., Li, A., Wei, B., Si, K., Wei, Y., Wang, X., Zhu, G., Chen, Q., Gu, X., et al. (2022). Electrochemical CO_2 reduction to ethylene by ultrathin CuO nanoplate arrays. Nat. Commun. *13*, 1877. https://doi.org/10.1038/s41467-022-29428-9.

24. Kopač, D., Likozar, B., and Huš, M. (2020). How size matters: electronic, cooperative, and geometric effect in perovskite-supported copper catalysts for CO_2 reduction. ACS Catal. *10*, 4092–4102. https://doi.org/10.1021/acscatal.9b05303.

25. Christensen, O., Zhao, S., Sun, Z., Bagger, A., Lauritsen, J.V., Pedersen, S.U., Daasbjerg, K., and Rossmeisl, J. (2022). Can the CO_2 reduction reaction be improved on Cu: selectivity and intrinsic activity of functionalized Cu surfaces. ACS Catal. *12*, 15737–15749. https://doi.org/10.1021/acscatal.2c04200.

26. Liu, F., and Fan, Z. (2023). Defect engineering of two-dimensional materials for advanced energy conversion and storage. Chem. Soc. Rev. *52*, 1723–1772. 10.1039/D2CS00931E. https://doi.org/10.1039/D2CS00931E.

27. Wakerley, D., Lamaison, S., Wicks, J., Clemens, A., Feaster, J., Corral, D., Jaffer, S.A., Sarkar, A., Fontecave, M., Duoss, E.B., et al. (2022). Gas diffusion electrodes, reactor designs and key metrics of low-temperature CO_2 electrolysers. Nat. Energy *7*, 130–143. https://doi.org/10.1038/s41560-021-00973-9.

28. Banerjee, S., Gerke, C.S., and Thoi, V.S. (2022). Guiding CO_2RR selectivity by compositional tuning in the electrochemical double layer. Acc. Chem. Res. *55*, 504–515. https://doi.org/10.1021/acs.accounts.1c00680.

29. Wang, J., Yang, H., Liu, Q., Liu, Q., Li, X., Lv, X., Cheng, T., and Wu, H.B. (2021). Fastening Br^- ions at copper–molecule interface enables highly efficient electroreduction of CO_2 to ethanol. ACS Energy Lett. *6*, 437–444. https://doi.org/10.1021/acsenergylett.0c02364.

30. Tan, X., Yu, C., Ren, Y., Cui, S., Li, W., and Qiu, J. (2021). Recent advances in innovative strategies for the CO_2 electroreduction reaction. Energy Environ. Sci. *14*, 765–780. https://doi.org/10.1039/d0ee02981e.

31. Yu, J., Yin, J., Li, R., Ma, Y., and Fan, Z. (2022). Interfacial electric field effect on electrochemical carbon dioxide reduction reaction. Chem Catal. *2*, 2229–2252. https://doi.org/10.1016/j.checat.2022.07.024.

32. Monteiro, M.C.O., Dattila, F., López, N., and Koper, M.T.M. (2022). The role of cation acidity on the competition between hydrogen evolution and CO_2 reduction on gold electrodes. J. Am. Chem. Soc. *144*, 1589–1602. https://doi.org/10.1021/jacs.1c10171.

33. Waegele, M.M., Gunathunge, C.M., Li, J., and Li, X. (2019). How cations affect the electric double layer and the rates and selectivity of electrocatalytic processes. J. Chem. Phys. *151*, 160902. https://doi.org/10.1063/1.5124878.

34. Singh, M.R., Kwon, Y., Lum, Y., Ager, J.W., and Bell, A.T. (2016). Hydrolysis of electrolyte cations enhances the electrochemical reduction of CO_2 over Ag and Cu. J. Am. Chem. Soc. *138*, 13006–13012. https://doi.org/10.1021/jacs.6b07612.

35. Ren, W., Xu, A., Chan, K., and Hu, X. (2022). A cation concentration gradient approach to tune the selectivity and activity of CO_2 electroreduction. Angew. Chem. Int. Ed. *61*, 202212329. https://doi.org/10.1002/anie.202214173.

36. Ringe, S., Clark, E.L., Resasco, J., Walton, A., Seger, B., Bell, A.T., and Chan, K. (2019). Understanding cation effects in electrochemical CO_2 reduction. Energy Environ. Sci. *12*, 3001–3014. https://doi.org/10.1039/c9ee01341e.

37. Ayemoba, O., and Cuesta, A. (2017). Spectroscopic evidence of size-dependent buffering of interfacial pH by cation hydrolysis during CO_2 electroreduction. ACS Appl. Mater. Interfaces *9*, 27377–27382. https://doi.org/10.1021/acsami.7b07351.

38. Resasco, J., Chen, L.D., Clark, E., Tsai, C., Hahn, C., Jaramillo, T.F., Chan, K., and Bell, A.T. (2017). Promoter effects of alkali metal cations on the electrochemical reduction of carbon dioxide. J. Am. Chem. Soc. *139*, 11277–11287. https://doi.org/10.1021/jacs.7b06765.

39. Moura de Salles Pupo, M., and Kortlever, R. (2019). Electrolyte effects on the electrochemical reduction of CO_2. ChemPhysChem *20*, 2926–2935. https://doi.org/10.1002/cphc.201900680.

40. Dunwell, M., Wang, J., Yan, Y., and Xu, B. (2017). Surface enhanced spectroscopic investigations of adsorption of cations on electrochemical interfaces. Phys. Chem. Chem. Phys. *19*, 971–975. https://doi.org/10.1039/c6cp07207k.

41. Dunwell, M., Yan, Y., and Xu, B. (2018). Understanding the influence of the electrochemical double-layer on heterogeneous electrochemical reactions. Curr. Opin. Chem. Eng. *20*, 151–158. https://doi.org/10.1016/j.coche.2018.05.003.

42. Mills, J.N., McCrum, I.T., and Janik, M.J. (2014). Alkali cation specific adsorption onto fcc(111) transition metal electrodes. Phys. Chem. Chem. Phys. *16*, 13699–13707. https://doi.org/10.1039/c4cp00760c.

43. Yasuda, S., Tamura, K., Kato, M., Asaoka, H., and Yagi, I. (2021). Electrochemically driven specific alkaline metal cation adsorption on a graphene interface. J. Phys. Chem. C *125*, 22154–22162. https://doi.org/10.1021/acs.jpcc.1c03322.

44. Sa, Y.J., Lee, C.W., Lee, S.Y., Na, J., Lee, U., and Hwang, Y.J. (2020). Catalyst-electrolyte interface chemistry for electrochemical CO_2 reduction. Chem. Soc. Rev. *49*, 6632–6665. https://doi.org/10.1039/d0cs00030b.

45. Zhao, G., and Zhu, H. (2020). Cation-π interactions in graphene-containing systems for water treatment and beyond. Adv. Mater. *32*, 1905756. https://doi.org/10.1002/adma.201905756.

46. Ovalle, V.J., Hsu, Y.-S., Agrawal, N., Janik, M.J., and Waegele, M.M. (2022). Correlating hydration free energy and specific adsorption of alkali metal cations during CO_2 electroreduction on Au. Nat. Catal. *5*, 624–632. https://doi.org/10.1038/s41929-022-00816-0.

47. Wu, M., Zhang, Z., Xu, X., Zhang, Z., Duan, Y., Dong, J., Qiao, R., You, S., Wang, L., Qi, J., et al. (2020). Seeded growth of large single-crystal copper foils with high-index facets. Nature *581*, 406–410. https://doi.org/10.1038/s41586-020-2298-5.

48. Ji, Y., Jin, Z., Li, J., Zhang, Y., Liu, H., Shi, L., Zhong, Z., and Su, F. (2016). Rambutan-like hierarchically heterostructured CeO_2-CuO hollow microspheres: facile hydrothermal synthesis and applications. Nano Res. *10*, 381–396. https://doi.org/10.1007/s12274-016-1298-0.

49. Ruan, Y.C., Xie, Y.M., Chen, X.L., Dong, L., Zhang, F.F., Yang, T.T., Luo, X.F., Cheng, M.Y., Yin, P.F., Dong, C.K., et al. (2022). Exposing Cu(100) surface via ion-implantation-induced oxidization and etching for promoting hydrogen evolution reaction. Langmuir *38*, 2993–2999. https://doi.org/10.1021/acs.langmuir.2c00083.

50. Duan, Y.X., Meng, F.L., Liu, K.H., Yi, S.S., Li, S.J., Yan, J.M., and Jiang, Q. (2018). Amorphizing of Cu nanoparticles toward highly efficient and robust electrocatalyst for CO_2 reduction to liquid fuels with high faradaic efficiencies. Adv. Mater. *30*, 1706194. https://doi.org/10.1002/adma.201706194.

51. Wu, Z.-Z., Zhang, X.-L., Niu, Z.-Z., Gao, F.-Y., Yang, P.-P., Chi, L.-P., Shi, L., Wei, W.-S., Liu, R., Chen, Z., et al. (2022). Identification of Cu(100)/Cu(111) Interfaces as superior active sites for CO dimerization during CO_2 electroreduction. J. Am. Chem. Soc. *144*, 259–269. https://doi.org/10.1021/jacs.1c09508.

52. Zhang, G., Zhao, Z.J., Cheng, D., Li, H., Yu, J., Wang, Q., Gao, H., Guo, J., Wang, H., Ozin, G.A., et al. (2021). Efficient CO_2 electroreduction on facet-selective copper films with high conversion rate. Nat. Commun.

12, 5745. https://doi.org/10.1038/s41467-021-26053-w.

53. Zhong, D., Zhao, Z.J., Zhao, Q., Cheng, D., Liu, B., Zhang, G., Deng, W., Dong, H., Zhang, L., Li, J., et al. (2021). Coupling of Cu(100) and (110) facets promotes carbon dioxide conversion to hydrocarbons and alcohols. Angew. Chem. Int. Ed. Engl. *60*, 4879–4885. https://doi.org/10.1002/anie.202015159.

54. Song, Y., Xu, B., Liao, T., Guo, J., Wu, Y., and Sun, Z. (2021). Electronic structure tuning of 2D metal (hydr)oxides nanosheets for electrocatalysis. Small *17*, 2002240. https://doi.org/10.1002/smll.202002240.

55. Monteiro, M.C.O., Dattila, F., Hagedoorn, B., García-Muelas, R., López, N., and Koper, M.T.M. (2021). Absence of CO_2 electroreduction on copper, gold and silver electrodes without metal cations in solution. Nat. Catal. *4*, 654–662. https://doi.org/10.1038/s41929-021-00655-5.

56. Murata, A., and Hori, Y. (1991). Product selectivity affected by cationic species in electrochemical reduction of CO_2 and CO at a Cu electrode. Bull. Chem. Soc. Jpn. *64*, 123–127. https://doi.org/10.1246/bcsj.64.123.

57. Peng, C., Yang, S., Luo, G., Yan, S., Shakouri, M., Zhang, J., Chen, Y., Li, W., Wang, Z., Sham, T.K., and Zheng, G. (2022). Surface co-modification of halide anions and potassium cations promotes high-rate CO_2-to-ethanol electrosynthesis. Adv. Mater. *34*, 2204476. https://doi.org/10.1002/adma.202204476.

58. Clark, S.J., Segall, M.D., Pickard, C.J., Hasnip, P.J., Probert, M.I.J., Refson, K., and Payne, M.C. (2005). First principles methods using CASTEP. Z. Kristallogr. *220*, 567–570. https://doi.org/10.1524/zkri.220.5.567.65075.

59. Perdew, J.P., Burke, K., and Ernzerhof, M. (1996). Generalized gradient approximation made simple. Phys. Rev. Lett. *77*, 3865–3868. https://doi.org/10.1103/PhysRevLett.77.3865.

60. Hasnip, P., and Pickard, C. (2006). Electronic energy minimisation with ultrasoft pseudopotentials. Comput. Phys. Commun. *174*, 24–29. https://doi.org/10.1016/j.cpc.2005.07.011.

61. Perdew, J.P., Chevary, J.A., Vosko, S.H., Jackson, K.A., Pederson, M.R., Singh, D.J., and Fiolhais, C. (1992). Atoms, molecules, solids, and surfaces: applications of the generalized gradient approximation for exchange and correlation. Phys. Rev. B Condens. Matter *46*, 6671–6687. https://doi.org/10.1103/physrevb.46.6671.

62. Head, J.D., and Zerner, M.C. (1985). A Broyden—fletcher—Goldfarb—shanno optimization procedure for molecular geometries. Chem. Phys. Lett. *122*, 264–270. https://doi.org/10.1016/0009-2614(85)80574-1.